Supplementary information for

Sub-1-volt, reconfigurable Gires-Tournois resonators for full-colour monopixel array

Joo Hwan Ko[1,2†], Hyo Eun Jeong[1†], Serim Kim[1], Doeun Kim[1,3], Se Yeon Kim[1], Young Jin Yoo[2], Hyeon-Ho Jeong[1,3,4*], Young Min Song[1,4,5,6*]

[1]*School of Electrical Engineering and Computer Science, Gwangju Institute of Science and Technology, Gwangju 61005, Republic of Korea.*

[2]*Department of Mechanical Engineering, Massachusetts Institute of Technology, Cambridge, Massachusetts 02139, USA*

[3]*GIST InnoCORE AI-Nano Convergence Initiative for Early Detection of Neurodegenerative Diseases, Gwangju Institute of Science and Technology, Gwangju 61005, Republic of Korea*

[4]*Department of Semiconductor Engineering, Gwangju Institute of Science and Technology, Gwangju 61005, Republic of Korea.*

[5]*AI Graduate School, Gwangju Institute of Science and Technology, Gwangju 61005, Republic of Korea.*

[6]*School of Electrical Engineering, Korea Advanced Institute of Science and Technology, Daejeon 34141, Republic of Korea.*

† *J. H. Ko and H. E. Jeong contributed equally to this work.*

*Corresponding author

E-mail: *jeong323@gist.ac.kr*; *ymsong@kaist.ac.kr*

Supplementary Note 1. Strategy of designing Gires-Tournois resonator with tri-layer structure to enhance sensitivity in optical modulation

To enhance chromaticity, resonance based optical modulators for full colour generation should be configured to be sensitive to modulation in low refractive index medium. As a simple method for the dynamic display involves using a Gires-Tournois resonator structure in a low refractive index medium, designed using transmission line theory, described by the following equation:

$$Z_{in} = Z_a \frac{Z_m + iZ_a \tan \beta_a t_a}{Z_a + iZ_m \tan \beta_a t_a} \tag{1}$$

Z_{in} is the input impedance of the system, where β_a represents the wavenumber in the low refractive index medium, specifically active layer, given by $2\pi n_a/\lambda$. The active layer and metal reflector are associated with impedances $Z_a = Z_0/n_a$ and $Z_m = Z_0/N_m$, where $N_m = n_m + ik_m$, respectively. Here, n_m and k_m are refractive index and extinction coefficient of the metal, and Z_0 is the impedance of free space. Therefore, the reflection coefficient r of incident light from air is given by

$$r = \frac{Z_{in} - Z_0}{Z_{in} + Z_0} \tag{2}$$

and when $R = 1$, unity absorption is achieved, resulting in impedance matching, i.e., $Z = Z_0$, and the absorption $A = 1 - R = 0$. To determine the values, Au layer was chosen as the metal reflector, and the low refractive index medium was set to approximately 1.5, similar to the refractive index of polyaniline (PANI). The impedance matching condition is then represented by a simple equation as a function of the dielectric layer thickness (t_a).

$$\tan\left(\frac{2\pi n_a t_a}{\lambda}\right) = i\frac{n_a(N_m + 1)}{N_m - {n_a}^2} \tag{3}$$

$$\mathrm{f}(t_a) = \tan\left(\frac{2\pi n_a t_a}{\lambda}\right) - i\frac{n_a(N_m + 1)}{N_m - {n_a}^2} \tag{4}$$

As shown by the simplified equation, the low refractive index medium contains only real values. Therefore, unity absorption cannot be achieved by varying thickness (t_a) if the imaginary part is not eliminated.

Lossy dielectrics with complex refractive indices produce significant phase shifts at the interface, making it challenging to predict the resonance condition. To address this, a low refractive index medium is required that can cancel the imaginary part through optical modulation. Consequently, the tri-layer structure is proposed as an improved design approach as shown in **Supplementary Figs. 3a and 3b**.

$$Z_{in,l} = Z_l \frac{Z_m + iZ_l \tan \beta_l t_l}{Z_l + iZ_m \tan \beta_l t_l} \tag{5}$$

$$Z_{in,a} = Z_a \frac{Z_{in,l} + iZ_a \tan \beta_a t_a}{Z_a + iZ_{in,l} \tan \beta_a t_a} \tag{6}$$

$$r = \frac{Z_{in,a} - Z_0}{Z_{in,a} + Z_0} \tag{7}$$

In low refractive index materials, a reduction in complex refractive index due to thickness changes is not typically applicable to most lossy materials. To achieve unity absorption, the complex refractive index must be modified through effective material engineering, such as controlling porosity (**Supplementary Fig. 3c**). Therefore, we selected Pr-Ge to achieve the impedance matching condition, resulting in single absorption (**Supplementary Fig. 4**). As a result, the designed resonator is highly sensitive to optical modulation in the active layer.

The effective index of the material is calculated based on the volume averaging theory (VAT). The effective refractive index (n_{eff}) and effective extinction coefficient (k_{eff}) of two-phase nanocomposite material can be determined as follows:

$$n_{eff}^2 = \frac{1}{2}\left[A + \sqrt{A^2 + B^2}\right] \tag{8}$$

$$k_{eff}^2 = \frac{1}{2}\left[-A + \sqrt{A^2 + B^2}\right] \tag{9}$$

where

$$A = \emptyset(n_d^2 - k_d^2) + (1 - \emptyset)(n_c^2 - k_c^2) \tag{10}$$

$$B = 2n_d k_d \emptyset + 2n_c k_c (1 - \emptyset) \tag{11}$$

The n_d and n_c represent the refractive indices of the continuous and dispersed phases, respectively, while k_d and k_c signify the extinction coefficients. The porosity is denoted by $\emptyset$. In this case, the dispersed phase is considered as vacuum, resulting in $n_d = 1$ and $k_d = 0$.

Supplementary Note 2. Wavelength tuning under negative group delay conditions with various redox states of PANI.

By utilising different redox states of PANI, the wavelength can be adjusted under negative group delay conditions in the *r*-GT structure, leading to significant shifts in the reflective wavelength. The *r*-GT configuration induces significant changes in the group velocity of light, enabling the observation of slow, fast, and negative group velocity phenomena. Negative group delay, where a light pulse appears to exit the medium before entering, is achieved through the resonant trapping of certain wavelengths within the spacer layer between the upper reflective surface and the underlying high reflector as shown in **Supplementary Figure 5**.

The refractive index and extinction coefficient of PANI vary with its redox state, enabling it to act as a tunable upper-surface reflector and leading to changes in resonance conditions (**Extended Data Fig. 2**). **In Figure 1f**, the scattered dots indicate the changes in the complex refractive index of PANI under different redox states. Compared to other configurations, the simulated reflectivity of the *r*-GT resonator reveals that the Pr-Ge structure effectively optimizes resonance conditions by fine-tuning its refractive index. **Figure 1g** shows reflectivity changes for different configurations: i) asymmetric Fabry–Pérot (F.-P.) resonator without Ge, where PANI is deposited directly onto the Au substrate; ii) Trilayer Gires-Tournois (GT) resonator with a-Ge incorporating a dense amorphous Ge layer inserted between Au and PANI; and iii) Tailored trilayer GT with Pr-Ge, consisting of a porous Ge layer between Au and PANI. Among these, the Pr-Ge structure exhibits the most pronounced resonance shift during the redox transition of PANI, indicating enhanced optical modulation performance.

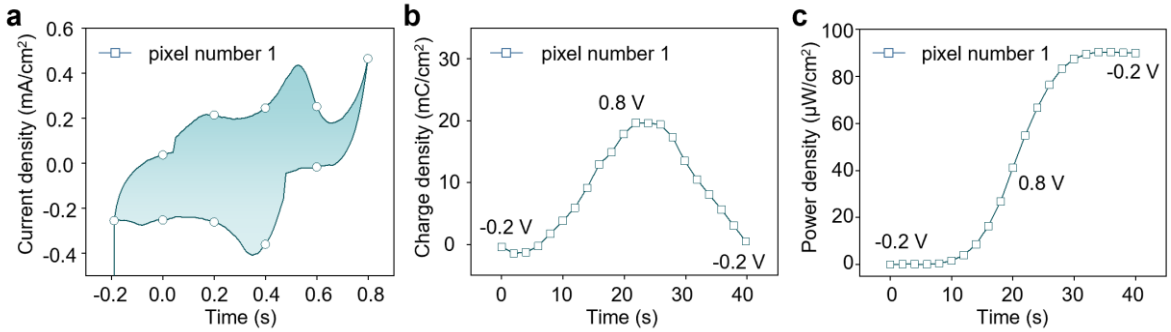

Supplementary Figure 1. Electrochemical performance of the *r*-GT monopixel during a single cycle. a, CV curve of *r*-GT monopixel in the addressable monopixel array. **b,** Reversible modulation of charge density during voltage sweep from -0.2 V to 0.8 V. **c,** Calculated power density consumed by *r*-GT resonator per cycle.

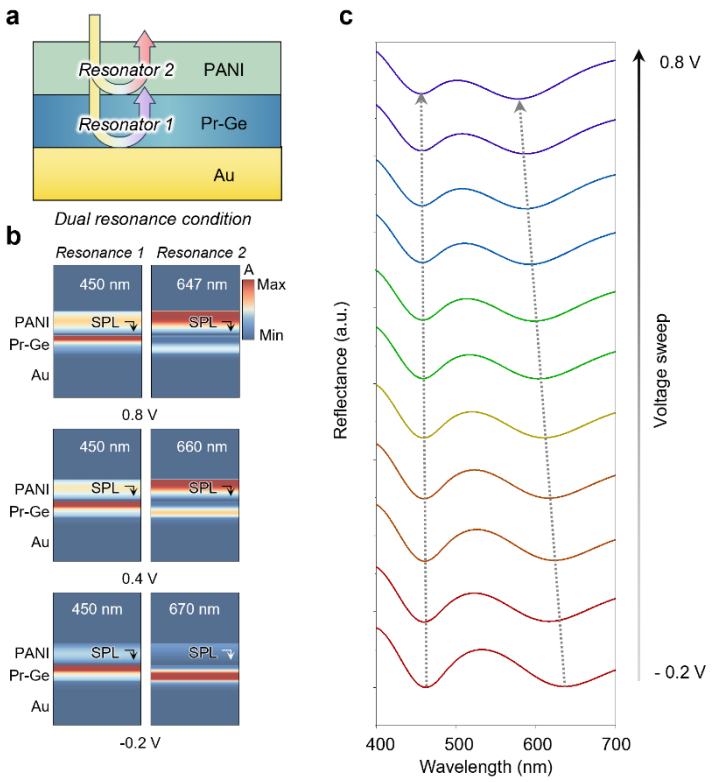

Supplementary Figure 2. **a**, Illustrations of the *r*-GT resonator under dual resonance conditions, showing the position of each resonance. **b**, Absorption profiles of *r*-GT monopixel at -0.2 V, 0.4 V, and 0.8 V. Under the reduced state (-0.2 V), the absorption in the PANI layer at the resonant wavelength decreases. **c,** Measured reflection spectra of *r*-GT in metallic state (0.8 V) and semiconducting state (-0.2 V) of PANI with voltage sweep at the corresponding visible range.

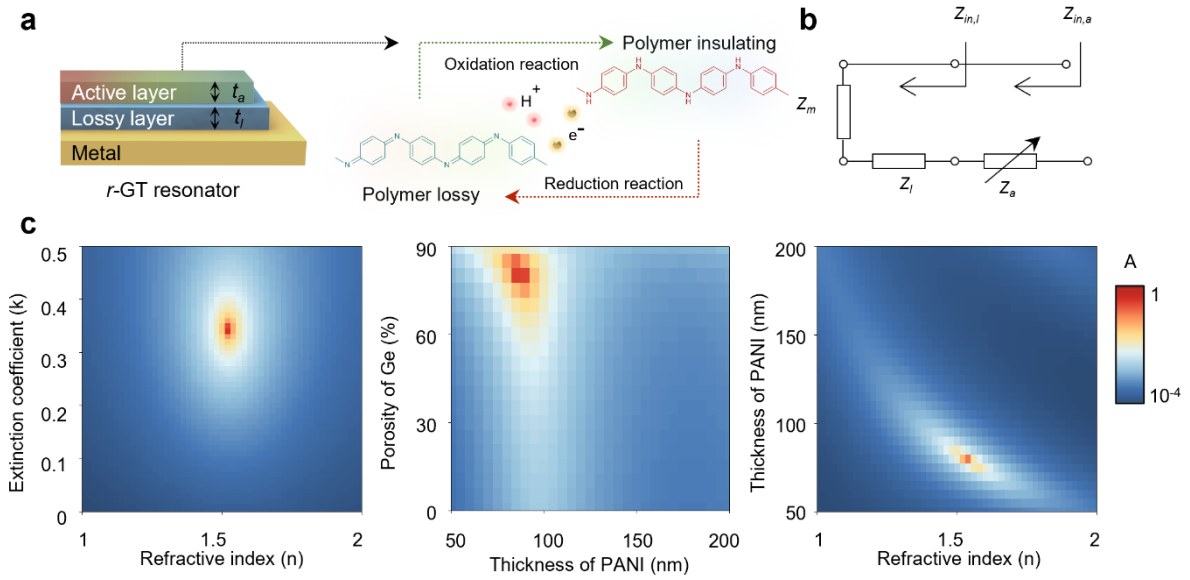

Supplementary Figure 3. Design of *r*-GT resonator for dynamic colour variation. a, Schematic illustration of the tri-layered optical resonator, where the complex refractive index of PANI changes through a redox reaction. **b,** Equivalent transmission line model of the tri-layered reconfigurable GT structure. The arrow indicates active modulation of the impedance in the active layer (PANI, Z_a). Z_l and Z_m represent impedance of lossy layer and metal layer, respectively. **c,** Absorption characteristics of the proposed design. Absorptance contour plots for varying thickness of PANI and porosity of Ge under resonant wavelength.

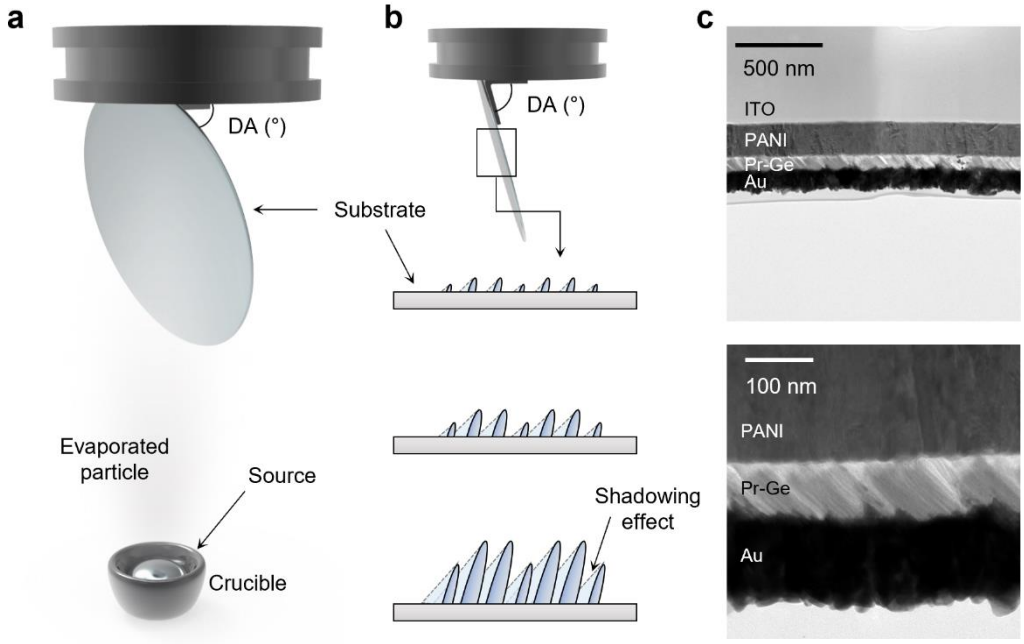

Supplementary Figure 4. Optical effect of porosity variation. a, Schematic of experimental setup with deposition angle (DA). **b,** Glancing angle deposition process of porous medium through the shadowing effect, resulting in modulation of the effective index as a porosity change. **c,** Transmission electron microscopy (TEM) image of the deposited morphology of Ge layer to modulate the porosity via e-beam evaporation. Scale bars are 500 nm (upper) and 100 nm (bottom).

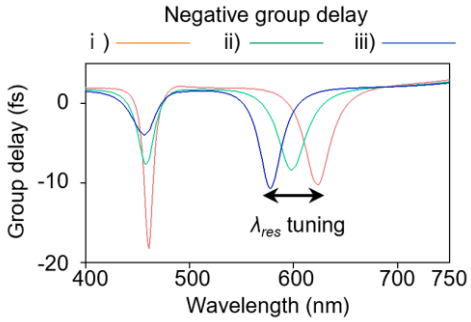

Supplementary Figure 5. Group delay response of *r*-GT across different voltage sweep ranges for various resonator configurations: i) asymmetric F.-P. cavity, ii) Trilayer GT resonator, and iii) Tailored trilayer GT resonator.

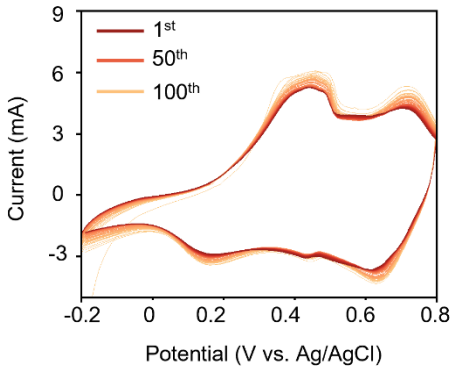

Supplementary Figure 6. Electrochemical stability of the *r*-GT resonator. The *r*-GT monopixel demonstrates stable redox reaction during 100 cycles.

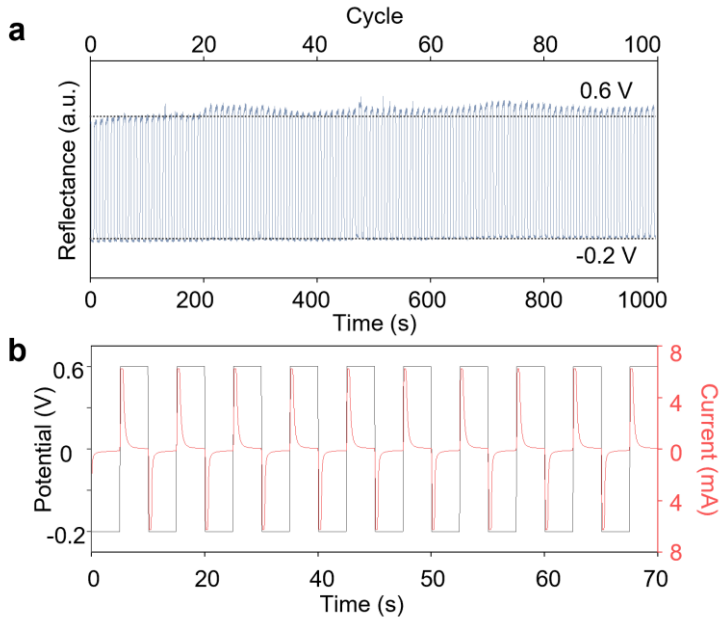

Supplementary Figure 7. Optical reversibility of *r*-GT resonator. a, Reflectance reversibility with bias voltage cycled from -0.2 V to 0.6 V (interval: 10 s) for 100 cycles. **b,** Measured current with applied voltage cycled from -0.2 V to 0.6 V. (interval: 10 s)

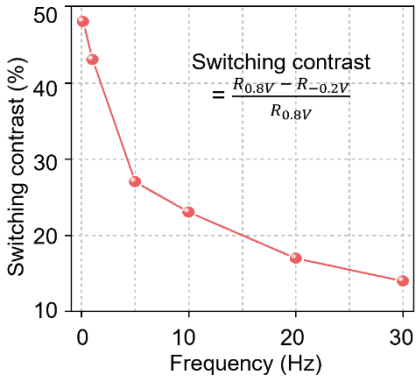

Supplementary Figure 8. Switching contrast of the *r*-GT resonator versus the applied frequency.

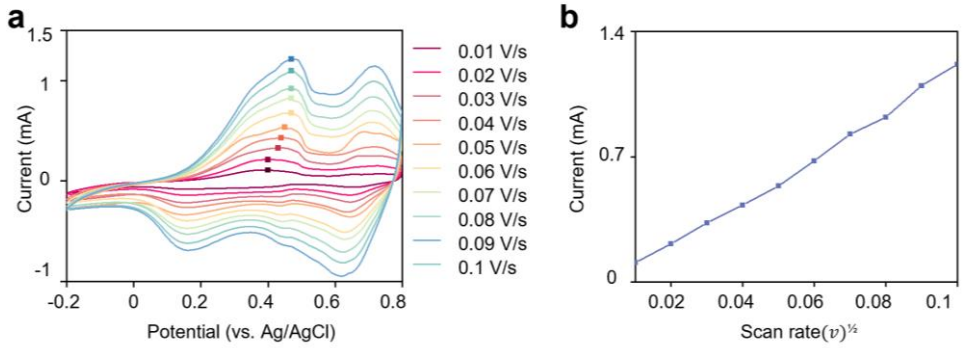

Supplementary Figure 9. Cyclic voltammetry of PANI. a, CV curve of PANI at different scan rates from 0.01 V/s to 0.1 V/s. **b,** The peak current of the first oxidation state increases with dependence on the scan rate by the following equation:

$$i_p = 0.4463\, nFAC \left(\frac{nFvD}{RT}\right)^{1/2} \tag{12}$$

Where the i_p is the current maximum of the CV curve, n is number of electrons transferred in the redox event, A is electrode area, F is Faraday's constant, D is diffusion coefficient, C is concentration of PANI, v is scan rate, R is Gas constant, and T is temperature. As a result, the i_p can be obtained from the slope of a plot against $\sqrt{v}$ at 25°C, using following equation:

$$i_p = 2.69 \times 10^5 n^{\frac{3}{2}} AC\sqrt{Dv} \sim \sqrt{v} \tag{13}$$

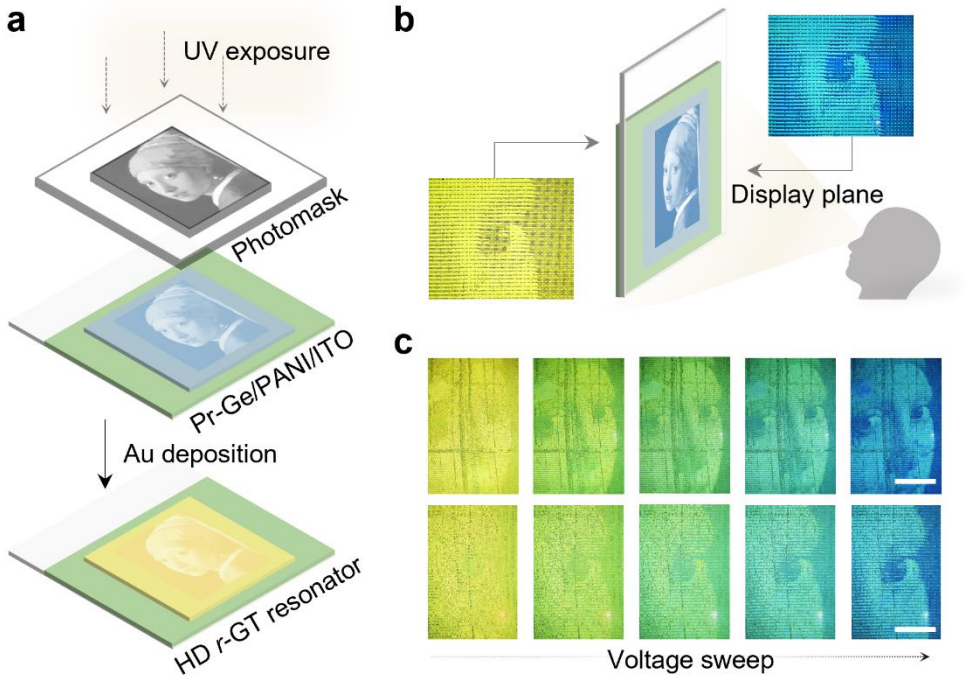

Supplementary Figure 10. High-density (HD) patterned *r*-GT resonator. a, Simplified fabrication process of HD *r*-GT monopixel array with prefabricated painting pattern from "*Girl with a pearl earring*". **b,** Optical microscopy image of high contrast pattern on the display plane. **c,** Visible modulation and magnified view of painting pattern with unit area during voltage sweep from -0.2 V to 0.8 V. Scale bar is 500 μm (top) and 250 μm (bottom).

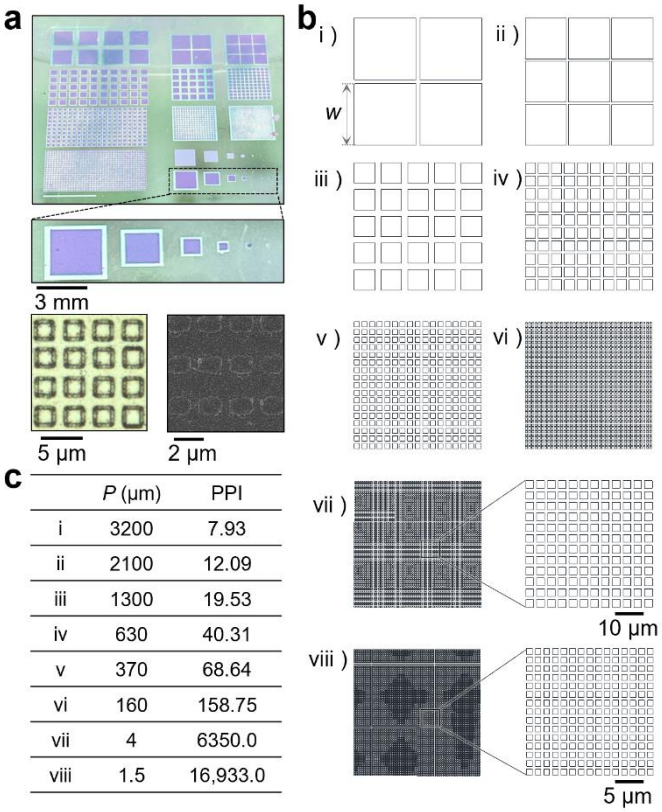

c

	P (μm)	PPI
i	3200	7.93
ii	2100	12.09
iii	1300	19.53
iv	630	40.31
v	370	68.64
vi	160	158.75
vii	4	6350.0
viii	1.5	16,933.0

Supplementary Figure 11. Design of the large-area, high-density *r*-GT monopixel array. **a,** Optical images and scanning electron microscope (SEM) image of fabricated large-area *r*-GT resonator used to calculate pixels per inch (PPI), along with a magnified view of the monopixels. **b,** Patterns designed for different pixel pitches (*P*), ranging from 3 mm to 1.5 μm (i-viii). **c,** PPI values calculated for each pixel pitch from 3200 μm to 1.5 μm shown in (b).

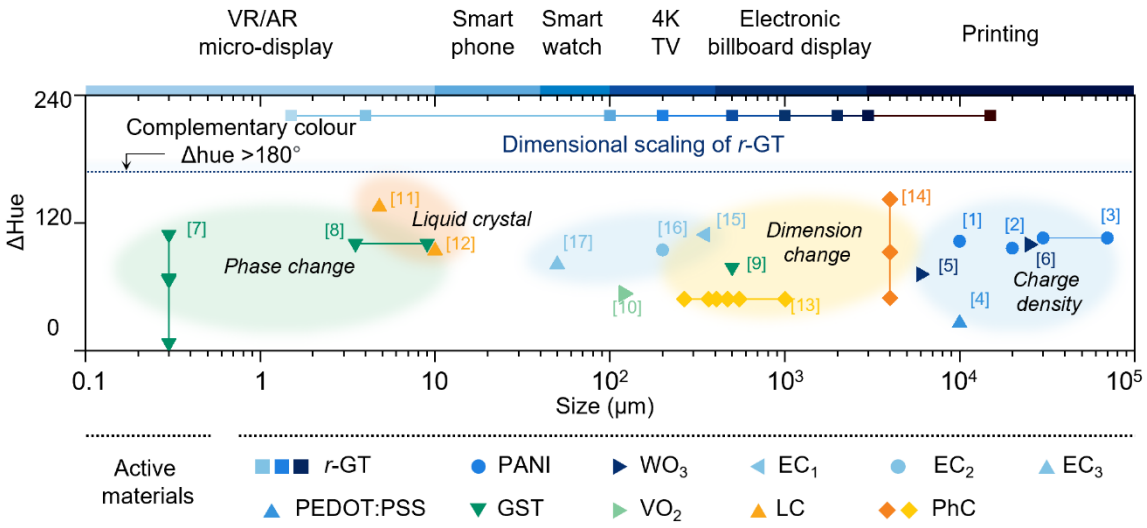

Supplementary Figure 12. Comparison of the hue range and pixel size across various active materials, including details about their modulation mechanisms as shown in Supplementary Table. 1[1-17].

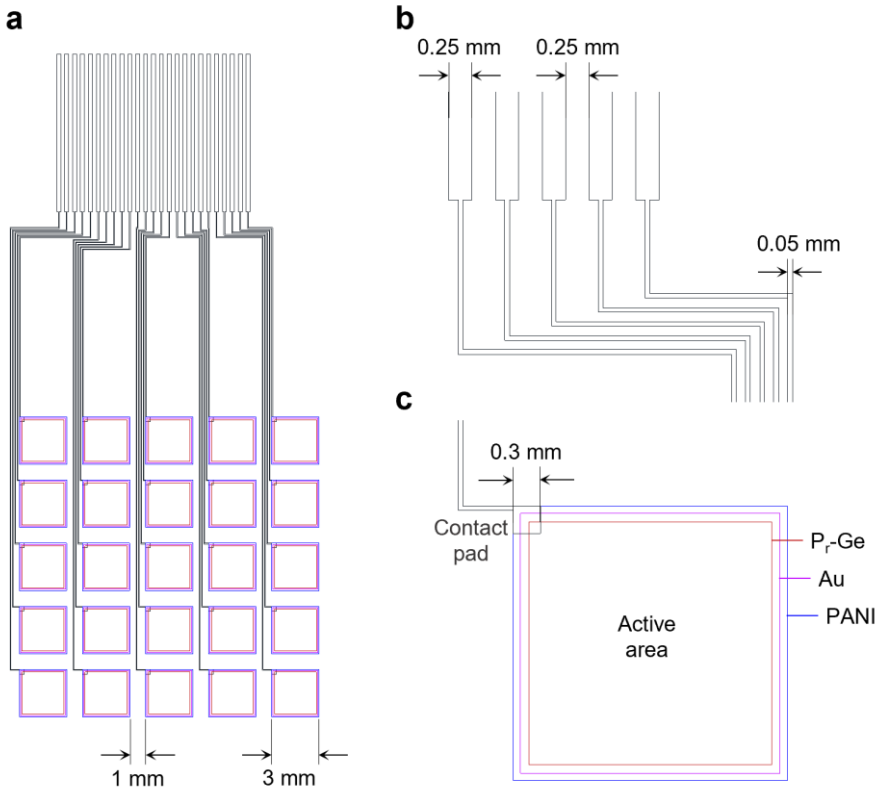

Supplementary Figure 13. Mechanical photomask design for the addressable monopixel array design. a, The design of *r*-GT monopixel array is configured using a passive matrix platform. The pixel size and spacing are defined as 3 mm and 1 mm, respectively, by shadow mask.. **b,** Electrode pattern design of *r*-GT monopixel array for connection with each pixel via photolithography. To enhance pixel density, the electrodes connected to the pixels were designed with a width of 0.05 mm, while the electrode width in the contact region for addressing through the control board was set to 0.25 mm. **c,** Active area definition of *r*-GT resonator. The electrode pattern included contact pads between the pixels and electrodes to improve stable electrochemical operation. The PANI region is in direct contact with the electrolyte to facilitate electrochemical operation via protonation. The Au reflector is designed to cover the Pr-Ge region to prevent the direct oxidation of Pr-Ge.

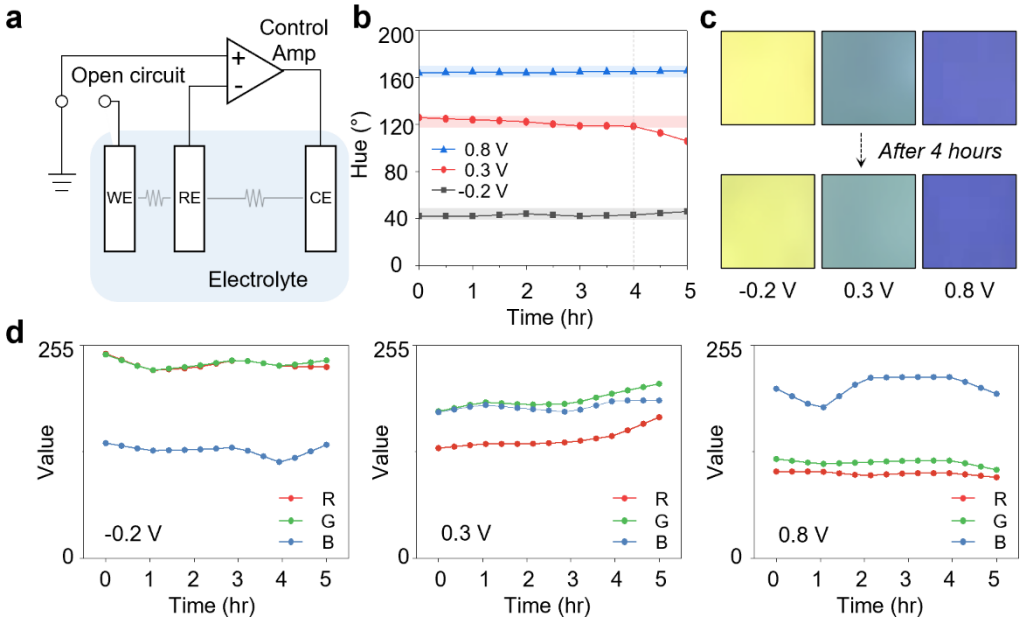

Supplementary Figure 14. Metastable properties of *r*-GT monopixel. a, Simplified potentiostat circuit diagram of three-electrodes system in an open-circuit state. In a three-electrode system, the working electrode (WE), reference electrode (RE), and counter electrode (CE) are connected indirectly through the electrolyte. The WE is short-circuited in the circuit after the measurement starts to demonstrate the metastable states. **b,** Optical memory effect of the *r*-GT monopixel at different voltages. In electrochemically stable states, such as 0.8 V and -0.2 V, the hue variation remains within 5 degrees over 5 hours. In contrast, at 0.3 V, significant colour degradation becomes apparent after 4 hours. **c,** Photographs of *r*-GT resonator after disconnecting the power supply and after 4 hours. **d,** RGB values calculated from the optical images at different voltages corresponding to (b).

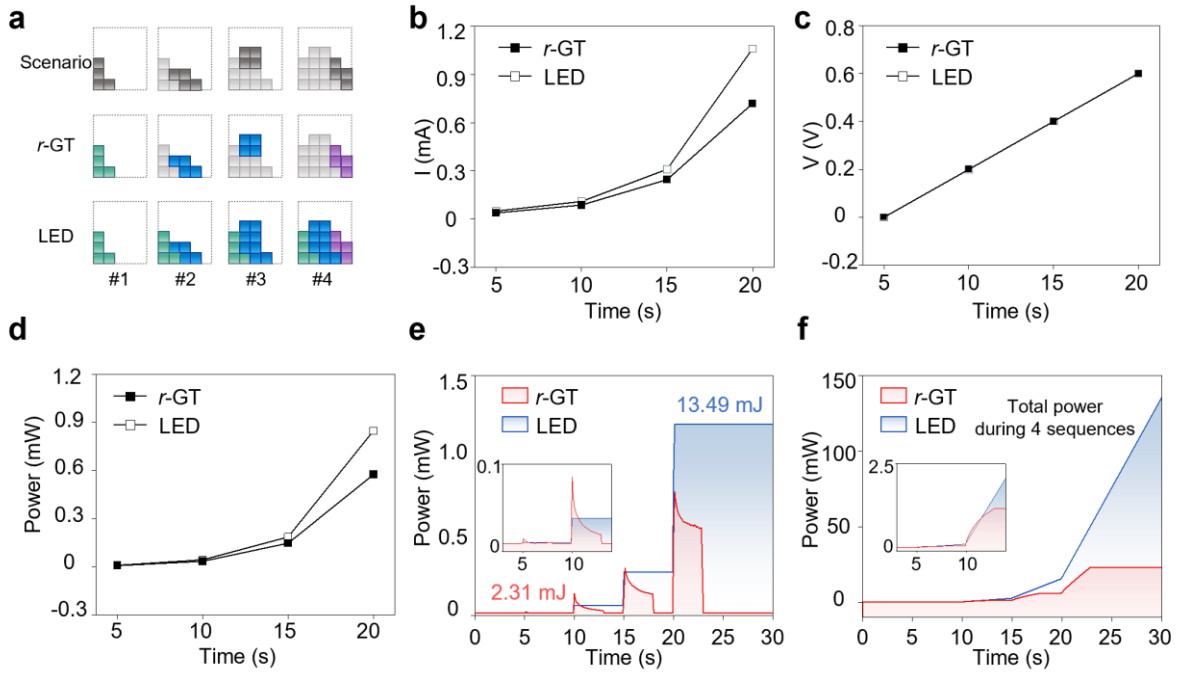

Supplementary Figure 15. Non-volatile properties of *r*-GT monopixel array. a, Schematics depicting a virtual scenario of the *"Tetris game"* and the time-dependent states displayed through *r*-GT and LED. The regions with coloured pixels consume power, while the gray pixels conserve electrical energy. The *r*-GT monopixels, with their optical memory properties, operate only the pixels that are progressively activated based on the scenario, while the volatile LED requires constant power to sustain all pixels. **b-c,** The measured current (b) and voltage (c) of the *r*-GT for colour display, compared to the typical voltage and current values of an LED. **d,** Calculated power corresponding to different current and voltage values, as shown in (b-c), by time delay. **e,** The changed power used to activate the added pixels and the total energy. **f,** Calculated total power of *r*-GT and LED for expressing the four-sequences. In comparison to the *r*-GT resonator, LED requires a continuous power supply due to optical volatile properties, resulting in significant power consumption.

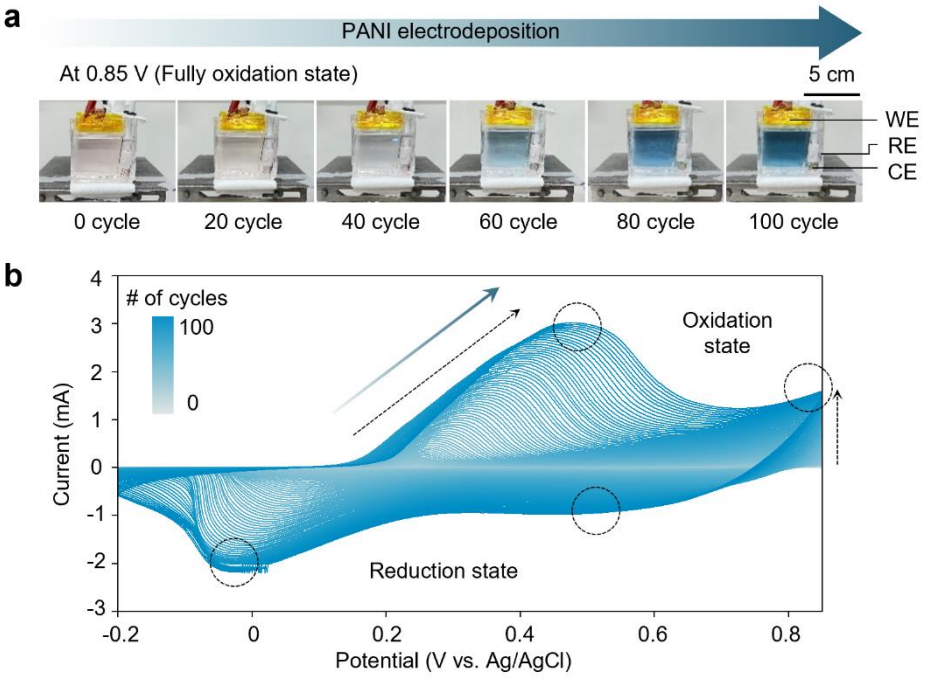

Supplementary Figure 16. Electrodeposition process of PANI. a, Photograph of the electrodeposition process of PANI during 100 cycles in 2 M HNO_3 and 70 mM aniline monomer. RE, CE, and WE are abbreviations for the reference electrode, counter electrode and working electrode, respectively. The scale bar is 5 cm. **b** The oxidation peaks of the cyclic voltammetric (CV) curve continuously increase due to the deposition of the PANI film.

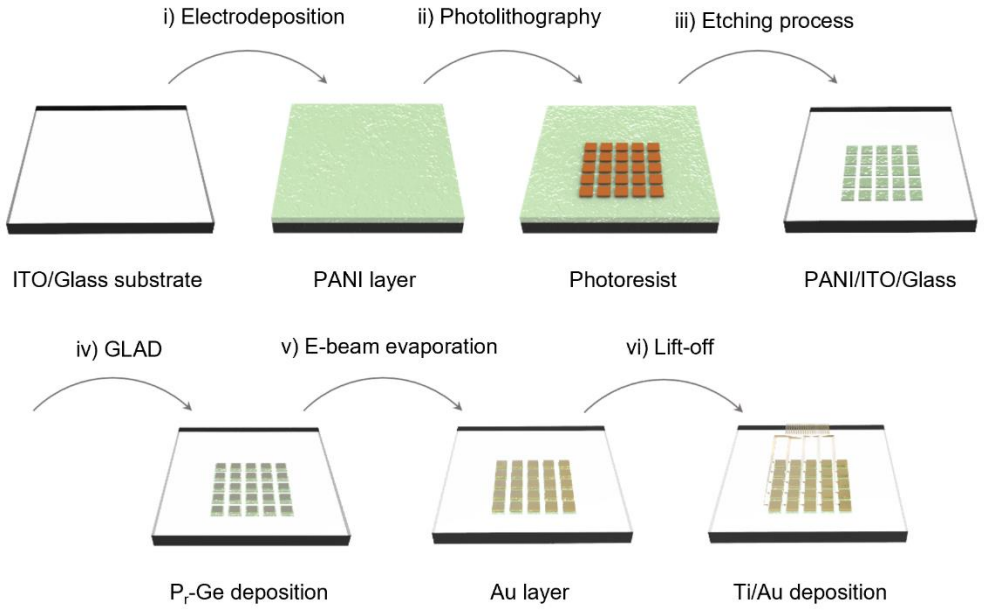

Supplementary Figure 17. Schematic illustration of a fabrication step for *r*-GT monopixel array. i) PANI layer is deposited using potentiostat on an ITO/Glass substrate. ii) The photoresist (PR) is patterned using a Cr photomask by photolithography process. iii) To define the isolated pixel area, the PANI layer is etched with O_2 plasma etching process, and 25 pixels are isolated through the ITO wet etching process. iv) To enhance chromaticity by utilising the impedance matching process, the porous (Pr) Ge layer is deposited by e-beam evaporation with glancing angle deposition (GLAD) method via a shadow mask. The *r*-GT resonator is configured with an ultrathin and highly lossy film under normal incidence, consisting of an air/absorber/metal mirror configuration. v) The Au layer, serving as the metal reflector, is deposited via e-beam evaporation using a shadow mask. vi) To individually control each pixel, image reversal PR pattern is formed with a Cr mask. Then, the Ti/Au electrodes are deposited with e-beam evaporator and patterned through lift-off process using acetone, where the the Ti layer serves as the adhesion layer.

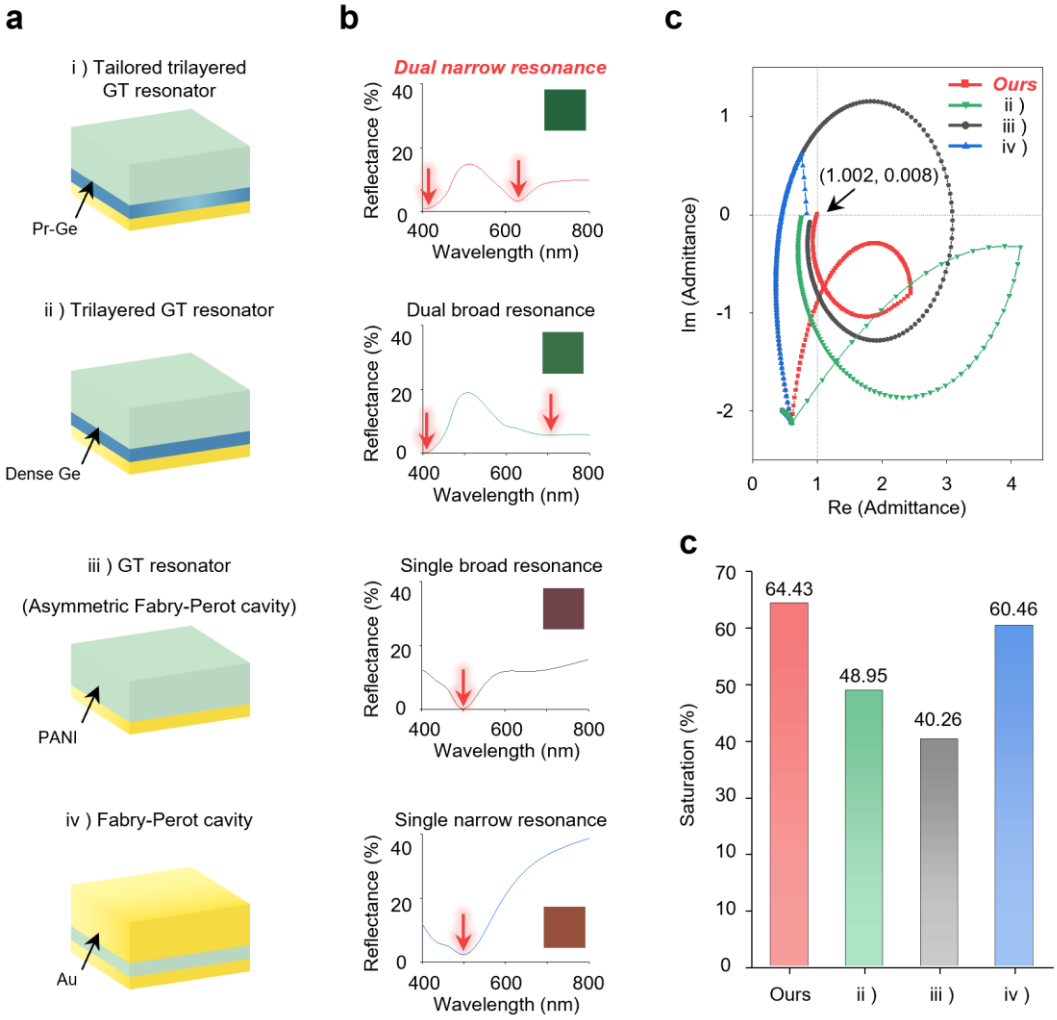

Supplementary Figure 18. Optical design strategies for enhanced colour quality. a, Schematics of photonic structures and their reflection spectra: i) Tailored trilayered GT resonator, ii) trilayered GT resonator, GT resonator, and Fabry-Parot cavity. **b,** Calculated admittance diagram for (i) to (iv) at each resonance wavelengths. **c,** Calculated saturation corresponding to (a). Both trilayered GT resonators enable additive colour generation in the visible range via dual resonance. However, design (i) with optimized porosity produces a deeper resonance dip, enhancing colour saturation.

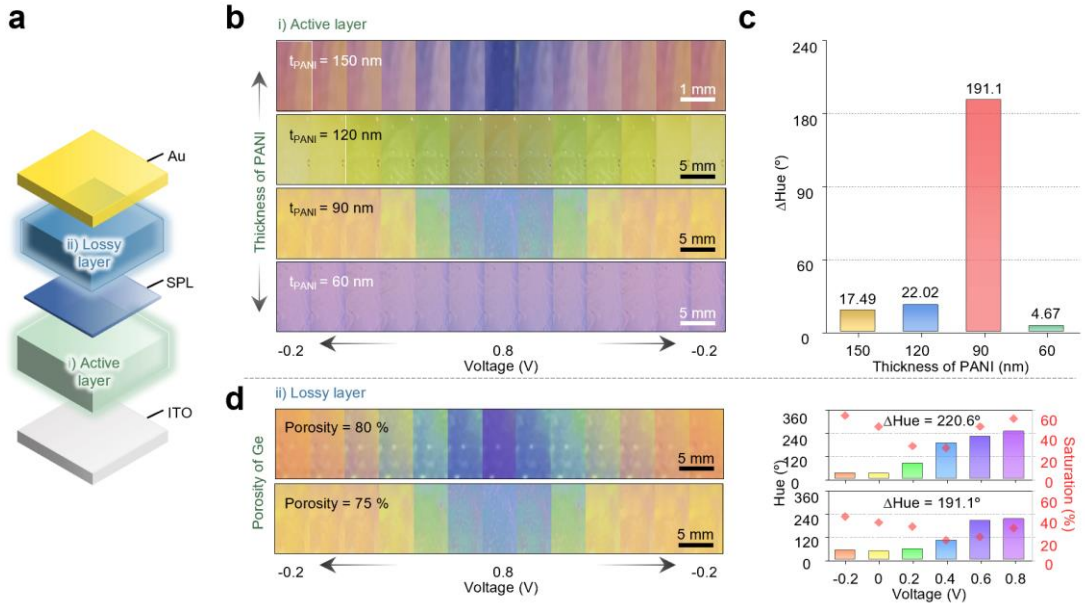

Supplementary Figure 19. Optical design optimization for enhanced hue range. a, Schematic illustration of each layer comprising the *r*-GT resonator. **b,** Photograph of reversible colour modulation corresponding to different thickness of active layers. **c,** Colour modulation range of the *r*-GT structures as a function of PANI thickness (150 nm, 120m, 90nm and 60 nm). **d,** Photographic images illustrating the colour changes of *r*-GT resonators with different porosities under varying applied voltages. **e,** Comparison of the hue and saturation values corresponding to the images in (d).

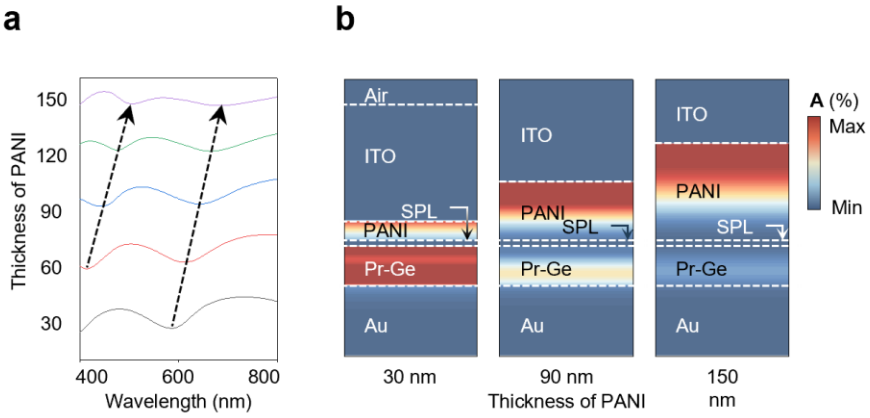

Supplementary Figure 20. Optimization strategy for dual-resonance spectral characteristics. a, Calculated reflectance spectra with varying PANI thickness in the visible range. **b,** Simulated absorption profiles at the resonant wavelengths for active layer thicknesses of 30 nm, 90 nm, and 150 nm.

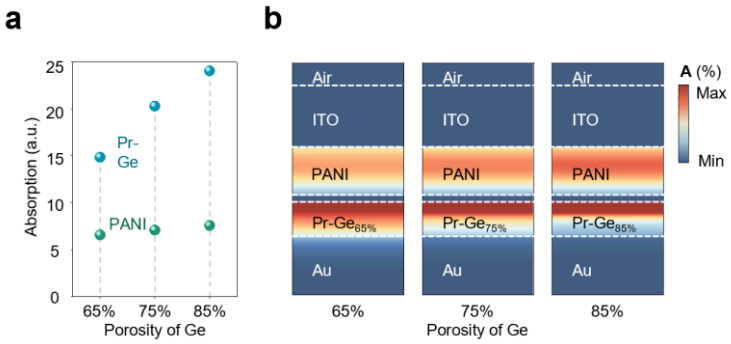

Supplementary Figure 21. Absorption characteristics depending on porosity of lossy layer. a, Calculated absorption in each layer (Pr-Ge and PANI) as a function of the porosity of the lossy medium. **b,** Simulated absorption profiles at the resonant wavelength for different porosities (Pr; 65%, 75% and 85 %).

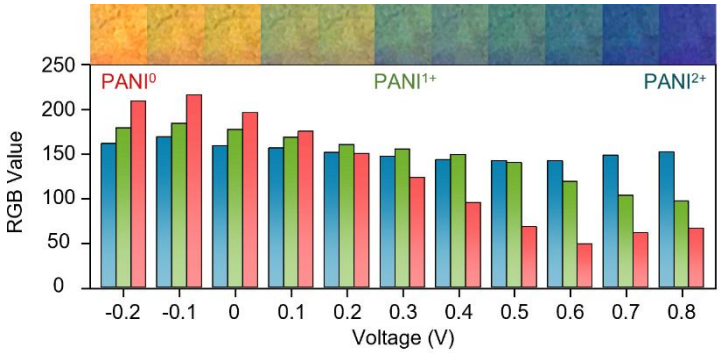

Supplementary Figure 22. RGB value variation of the *r*-GT resonator as a function of applied potential. Electrochemically induced RGB variation of the *r*-GT resonator under applied bias. The chemical state at -0.2 V corresponds to the fully reduced state ($PANI^{0}$) of PANI, while that at 0.8 V represents the fully oxidized state ($PANI^{2+}$).

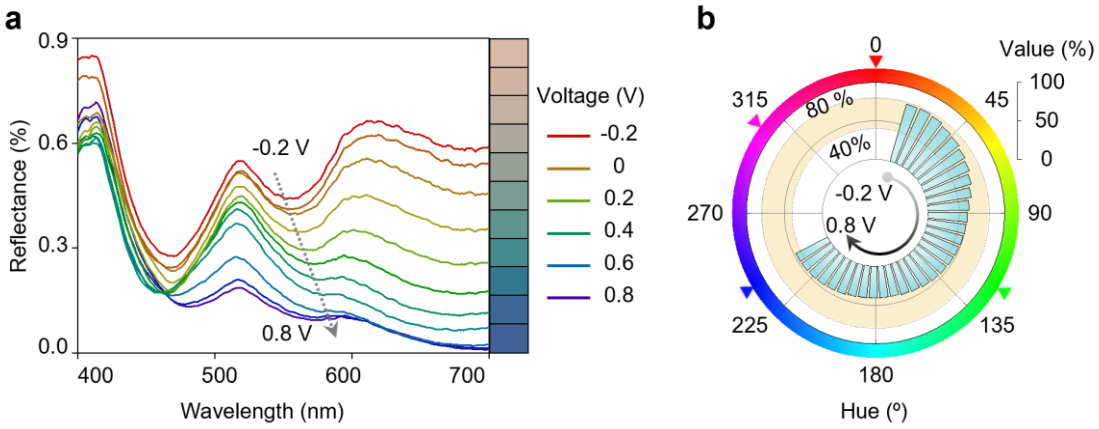

Supplementary Figure 23. Voltage-dependent colour modulation characteristics of the *r*-GT monopixel. a, Measured reflectance spectra and corresponding colour palette under varying applied voltages. The dual-resonance configuration produces two distinct dips within the visible spectrum, enabling adaptive colour modulation. **b,** Polar plot of the reflected hue and value extracted from the measured spectra as a function of applied voltage. The device maintains a value (brightness) above 40% across a wide hue modulation range (220.6°).

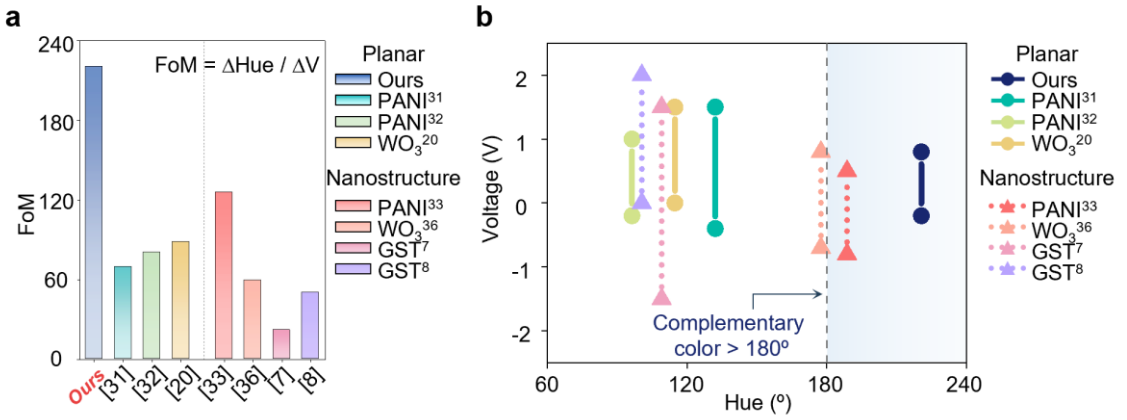

Supplementary Figure 24. Comparison of colour modulation range and voltage range in electrochromic resonators[7-8, 20, 31-33, 36]. a, Comparison of the figure of merit (FoM = Δhue/ΔV) between this device and reported electrochromic resonators [ref]. **b,** Comparison of hue range and applied voltage range. The blue box means colour modulation range exceeding complementary colours (>180°).

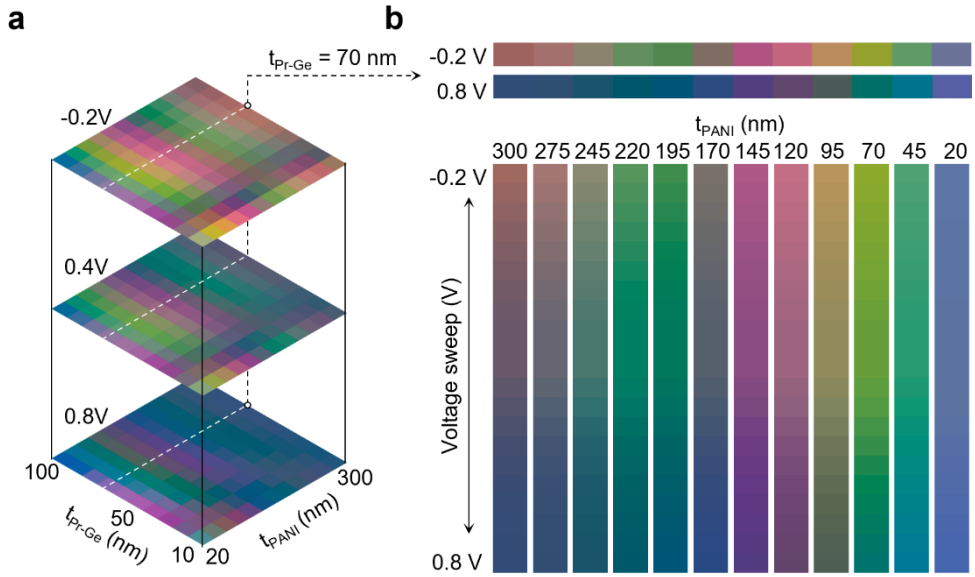

Supplementary Figure 25. colour modulation in tailored trilayer GT resonators. a, Voltage-dependent reflectance colour charts of tailored trilayer GT resonators (Au/Pr-Ge/PANI/ITO) as a function of Pr-Ge and PANI thicknesses. b, Representative colour palette is shown for a fixed Pr-Ge thickness of 70 nm, with variation in PANI thickness and applied voltage.

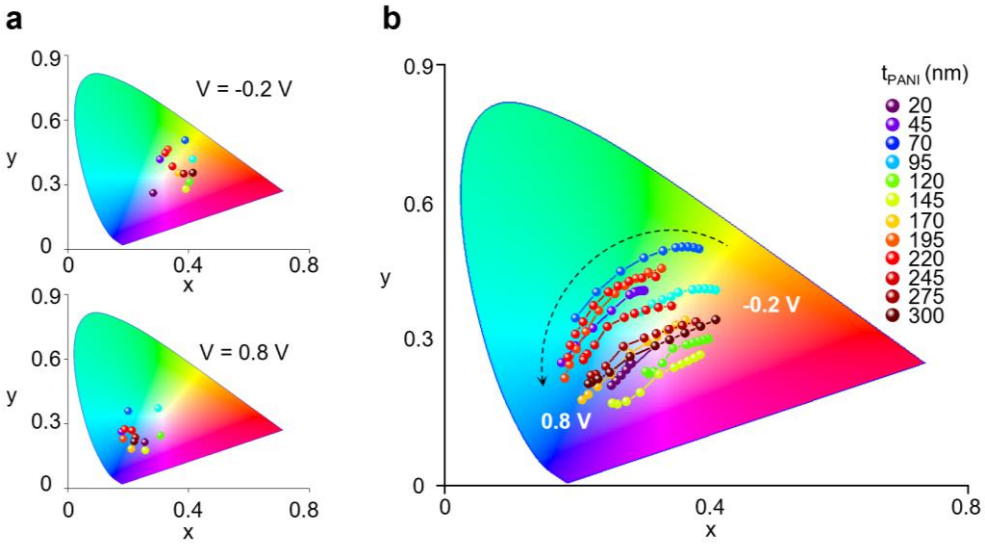

Supplementary Figure 26. CIE 1931 chromaticity coordinates of the *r*-GT resonator under various applied potentials. a, Chromaticity coordinates and sRGB coverage at fully reduced (-0.2 V) and fully oxidized (0.8 V) states for different PANI thicknesses. **b,** CIE colour coordinates for *r*-GT resonator with varying PANI thickness under applied voltage range -0.2V to 0.8 V in steps of 0.1 V.

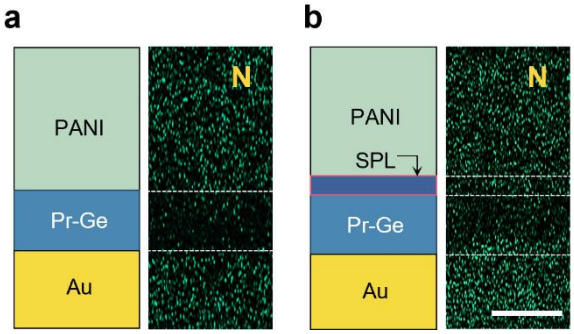

Supplementary Figure 27. EDS mapping of nitrogen before (a) and after (b) the first oxidation process. The elemental profile at the PANI/Pr-Ge interface shows an increased nitrogen concentration, attributed to doping and dedoping processes.

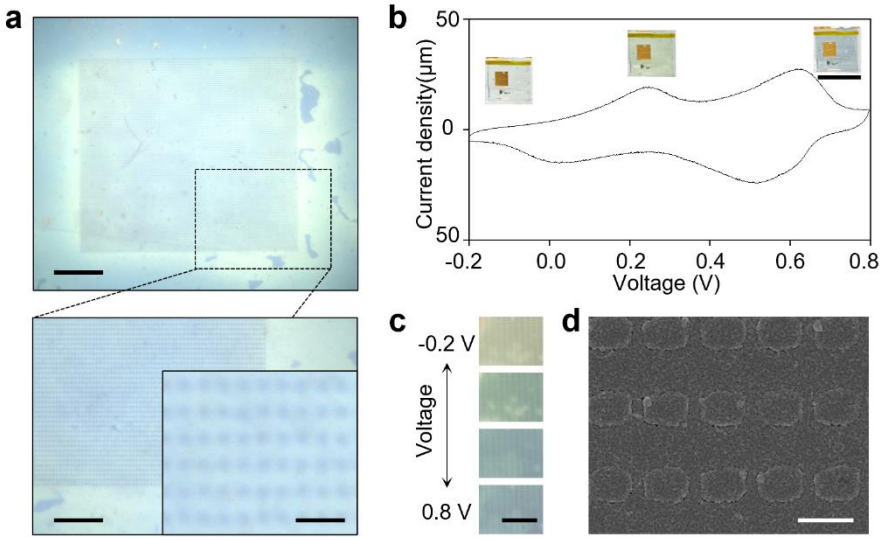

Supplementary Figure 28. Electrochemical characterization of micropixel *r*-GT resonator. a, Optical microscope (OM) images of the *r*-GT micropixel structure at different magnifications. Scale bars are 50 μm, 20 μm, and 5 μm. **b,** Cyclic voltammetry curve of the micropixel *r*-GT under electrochemical operation and a photograph of the actual sample. Scale bar is 1 cm. **c,** OM images of the micropixel under applied potentials, showing voltage-dependent colour modulation. Scale bar is 10 μm. **d,** Scanning electron microscope (SEM) image of the *r*-GT micropixel structure. Scale bar is 1.5 μm.

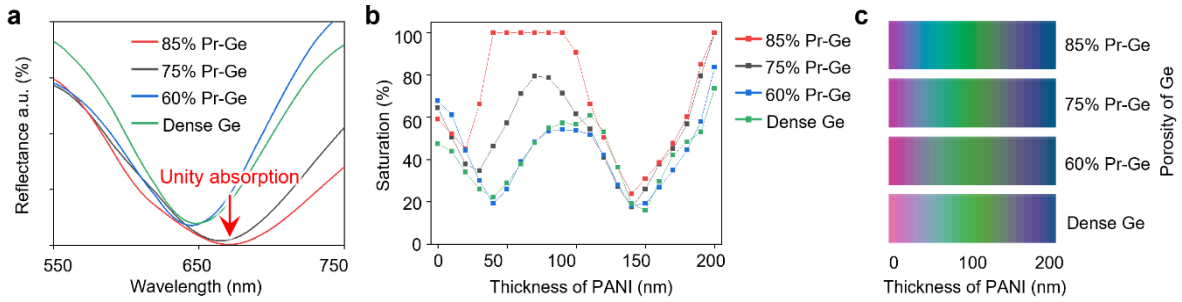

Supplementary Figure 29. Optimization of colour modulation and saturation by controlling Ge layer porosity a, Calculated reflectance spectra of GT resonator as a function of Ge layer porosity (dense, 60%, 75%, and 85%). **b,** Comparison of calculated reflected colour saturation with varying Ge porosity. The *r*-GT structure with 85% Pr-Ge achieves near-unity absorption and the highest colour saturation; however, considering fabrication feasibility, we optimized the design using 75% Pr-Ge. **c,** Colour chart showing the simulated visible colours as a function of PANI thickness under each porosity condition.

Active material	Tuning mechanism	Voltage (V)	Hue (°)	Ref.
PANI	Electrochemical doping	1.1	21.73	[18]
		2.5	102.76	[1]
		3	96.24	[2]
		5	105.78	[3]
PEDOT:PSS	Electrochemical doping	2.2	98.94	[19]
		6	25.81	[4]
WO_3	Electrochemical doping	1.3	31.39	[20]
		1.3	110.41	
		0.8	93.83	[21]
		0.8	76.93	
		3	71.73	[5]
		1.2	99.62	[6]
		1.6	46.60	[22]
P3MT/PB	Electrochemical doping	2	160.76	[23]
V_2O_5	Electrochemical doping	2.8	56.84	[24]
GST	Phase transition	5	68.14	[7]
		5	7.16	
		5	109.07	
		5	66.45	
		4	100.56	[8]
		10	78.29	[9]
VO_2	Phase transition	2	53.42	[10]
AIST	Phase transition	10	2.99	[25]
		10	120.52	
		10	30.77	
PhC	Particle rearrangement	7	48.93	[13]
		3.5	49.41	[14]
		3.5	92.41	
		3.5	141.90	
PANI	**Electrochemical doping**	**1**	**220.67**	**This work**

Supplementary Table 1. Comparison of active materials used in tunable photonics with the *r*-GT resonator based on voltage range and hue modulation[1-10, 13, 14, 18-25].

Active material	Mechanism	ΔHue (°)	ΔV (V)	# of states	# of pixels	Retention time (hr)	Min. pixel size (μm)	ref
GST	Phase transition	78.29	10	2	4	∞	500	[9]
VO_2	Phase transition	53.42	2	60	144	0	120	[10]
PhC	Particle rearrangement	48.39	7	2	7	-	1800	[13]
EC	Electrochemical doping	160.76	2	3	36	1	5000	[23]
EPD	Electrophoretic particle rearrangement	38.98	15	5	67200	∞	176	[26]
PANI	**Electrochemical doping**	**220.67**	**1**	**100**	**25**	**15**	**5**	**This work**

Supplementary Table 2. Comparison of reported tunable photonics and commercial displays comparing display performance data of six factors[9, 10, 13, 23, 26].

Types of cation	Hue range (°)	Response time (s)	Reversibility
H^+	**220**	**0.034**	**200**
Na^+	13	17.3	5
K^+	8	21.3	5

Supplementary Table 3. Comparison of optical properties of *r*-GT resonator in different electrolytes based on H^+, Na^+, and K^+.

Active material	Hue range	Pixel size (μm)	Ref.
PANI	102.76	10000	[1]
	96.24	20000	[2]
	105.78	30000	[3]
PEDOT:PSS	25.81	10000	[4]
WO_3	71.73	6000	[5]
	99.62	25000	[6]
GST	68.14	0.3	[7]
	7.16		
	109.07		
	66.45		
	100.56	9	[8]
		3.5	
	78.29	500	[9]
VO_2	53.42	120	[10]
LC	93.99	10	[11]
	135.08	4.8	[12]
PhC	48.39	1005	[13]
		549	
		471	
		407	
		366	
		266	
	49.41	4000	[14]
	92.41		
	141.90		
EC_1	108.88	350	[15]
EC_2	94.55	200	[16]
EC_3	81.02	50	[17]
PANI	**220.67**	**1.5**	**This work**
		4	
		100	
		200	
		500	
		1000	
		2000	
		3000	
		15000	

Supplementary Table 4. Comparison of pixel size and hue modulation in reported electrically responsive photonic devices[1-17].

Type	Active material	Structure		ΔHue (°)	ΔV (V)	FoM	Ref.
CP	**PANI**	**Planar**	**ITO glass/PANI/Pr-Ge/Au**	**220.67**	**1**	**220.67**	**Ours**
CP	PANI		antibody/PANI/ITO SPE	132.09	1.9	69.52	[31]
CP	PANI		CV-GS PANI/ITO/PET	96.32	1.2	80.27	[32]
Oxide	WO_3		WO_3/W	114.73	1.3	88.26	[20]
CP	PANI	**Nanostructure**	Nanoparticle	188.75	1.5	125.83	[33]
Oxide	WO_3		Nanohole	177.51	3	59.17	[36]
PCM	GST		Conductive Atomic Force Microscopy	109.07	5	21.81	[7]
PCM	GST		Conductive Atomic Force Microscopy	100.56	2	50.28	[8]

Supplementary Table 5. Comparison of optical performance between planar and nanostructured resonators, specifically in terms of hue range and operating voltage (FOM = ΔHue/ΔV)[7-8, 20, 31-33, 36].

Type	Active material		Structure	ΔHue (°)	ΔV (V)	Ref.
CP	**PANI**		**ITO glass/PANI/Pr-Ge/Au**	**220.6741**	**1**	**Ours**
CP	T34bT		Glass/Cr/Au/T34bT/Al	177.4432	1.7	[27]
CP	PANI		antibody/PANI/ITO SPE	132.0991	1.9	[31]
CP	PANI	**Planar**	CV-GS PANI/ITO/PET	96.32485	1.2	[32]
CP	PEDOT:PSS		PET/Ag electrode/electrolyte/CE	On/off	5	[35]
Oxide	WO_3		WO_3/W	114.7382	1.3	[20]
PCM	GST		Ag/Sb2S3/Ag/GST	77.12241	10	[9]
CP	T34bT		Nanohole	CIE	1.6	[27]
CP	$PProDOTMe_2$		Nanocave	157.3991	1.3	[28]
CP	Li_xSi		Metasurface	89.92093	1.49	[29]
CP	Ag^+		Nanodome	236.1534	1.5	[30]
LC	LC		Imprinted plasmonic surface	56.25076 126.5371	50	[34]
CP	PANI		Nanoparticle	188.7531	1.5	[33]
Oxide	WO_3	**Nanostructure**	Nanohole	177.5193	3	[36]
PCM	GST		Conductive Atomic Force Microscopy	68.14034 7.16839 109.0725 66.45099	5	[7]
PCM	GST		Metasurface	29.30854	Current pulse	[37]
PCM	GST		Conductive Atomic Force Microscopy	100.565	2	[8]

*CP: conductive polymer

*PCM: Phase change materials

*LC: Liquid Crystal

Supplementary Table 6. Comparison of hue modulation range (ΔHue) and operating voltage range (ΔV) between reported planar and nanostructured resonators[7-9, 20, 27-37].

Reference

1. Park, H. et al. A skin-integrated transparent and stretchable strain sensor with interactive a-changing electrochromic displays. *Nanoscale* **9**, 7631-7640 (2017).
2. Liu, G., Wang, Z., Wang, J., Liu, H. & Li, Z. Employing polyaniline/viologen complementarity to enhance coloration and charge dissipation in multicolor electrochromic display with wide modulation range. *J. Colloid Interface Sci.* **655**, 493-507 (2024).
3. Gong, H. et al. Ultrathin flexible electrochromic devices enabled by highly transparent ion-conducting films. *J. Mater. Chem. A* **11**, 8939-8949 (2023).
4. Brooke, R., Petsagkourakis, I., Wijeratne, K. & Andersson Ersman, P. Electrochromic displays manufactured by a combination of vapor phase polymerization and screen printing. *Adv. Mater. Technol.* **7**, 2200054 (2022).
5. Li, Y. et al. Colorful electrochromic displays with high visual quality based on porous metamaterials. *Adv. Mater.* **35**, 2300116 (2023).
6. Zhang, W., Li, H. & Elezzabi, A.Y. Electrochromic displays having two-dimensional CIE color space tunability. *Adv. Funct. Mater.* **32**, 2108341 (2022).
7. Hosseini, P., Wright, C.D. & Bhaskaran, H. An optoelectronic framework enabled by low-dimensional phase-change films. *Nature* **511**, 206-211 (2014).
8. Yoo, S., Gwon, T., Eom, T., Kim, S. & Hwang, C.S. Multicolor changeable optical coating by adopting multiple layers of ultrathin phase change material film. *ACS Photonics* **3**, 1265-1270 (2016).
9. Prabhathan, P., Sreekanth, K.V., Teng, J. & Singh, R. Electrically tunable steganographic nano-optical coatings. *Nano Lett.* **23**, 5236-5241 (2023).
10. Guo, T. et al. Durable and programmable ultrafast nanophotonic matrix of spectral pixels. *Nat. Nanotechnol.*, 1-9 (2024).
11. Franklin, D. et al. Polarization-independent actively tunable colour generation on imprinted plasmonic surfaces. *Nat. Commun.* **6**, 7337 (2015).
12. Huang, M. et al. Dynamically Tunable Structural Colors Enabled by Pixelated Programming of Soft Materials on Thickness. *Adv. Opt. Mater.* **11**, 2300573 (2023).
13. Fu, Q., Yu, W., Bao, G. & Ge, J. Electrically responsive photonic crystals with bistable states for low-power electrophoretic color displays. *Nat. Commun.* **13**, 7007 (2022).
14. Fu, Q., Zhu, H. & Ge, J. Electrically tunable liquid photonic crystals with large dielectric contrast and highly saturated structural colors. *Adv. Funct. Mater.* **28**, 1804628 (2018).
15. Xu, L.-J., Li, B., Gao, G.-L. & Jiang, Z. A metallosupramolecular polymer deposited via inkjet printing for fast-switching pixelated electrochromic devices. *J. Mater. Chem. C* **10**, 3353-3359 (2022).
16. Olsson, O., Gugole, M., Blake, J.C., Chukharkin, M. & Dahlin, A. Electrochromic active matrix with plasmonic metasurfaces. *RSC Appl. Interfaces* **1**, 719 (2024).
17. Moon, C.W., Kim, Y. & Hyun, J.K. Active electrochemical high-contrast gratings as on/off switchable and color tunable pixels. *Nat. Commun.* **13**, 3391 (2022).
18. Peng, J. et al. Scalable electrochromic nanopixels using plasmonics. *Sci. Adv.* **5**, eaaw2205 (2019).
19. Rekha, S., Joseph, T., Sengottaiyan, M. & Anil, K. ITO-Free Solution-Processed Flexible Electrochromic Devices Based on PEDOT: PSS as Transparent Conducting Electrode. *ACS Appl. Mater. Interfaces* **9**, 19427–19435 (2017).
20. Wang, Z. et al. Towards full-colour tunability of inorganic electrochromic devices using ultracompact fabry-perot nanocavities. *Nat. Commun.* **11**, 302 (2020).
21. Wu, Q. et al. Electrochromic metamaterials of metal–dielectric stacks for multicolor displays with high color purity. *Nano Lett.* **21**, 6891-6897 (2021).
22. Chen, J. et al. Reversible active switching of Fano and Fabry–Pérot resonances by electrochromic operation. *Laser Photon. Rev.* **16**, 2200303 (2022).
23. Kim, D.S. et al. Low power stretchable active-matrix red, green, blue (RGB) electrochromic device array of poly (3-methylthiophene)/Prussian blue. *Appl. Surf. Sci.* **471**, 300-308 (2019).
24. Mjejri, I., Rougier, A. & Gaudon, M. Low-cost and facile synthesis of the vanadium oxides V2O3, VO2, and V2O5 and their magnetic, thermochromic and electrochromic properties. *Inorg. Chem.* **56**, 1734-1741 (2017).
25. Ríos, C., Hosseini, P., Taylor, R. & Bhaskaran, H. Color depth modulation and resolution in Phase-Change Material nano-displays. *Adv. Mater.* **28** (2016).
26. Zang, H. et al. Electrophoretic display comprising black, white, red, and yellow particles. *J. Soc. Inf. Disp.* **30**, 387-394 (2022).
27. Rossi, S. et al. Dynamically tuneable reflective structural coloration with electroactive conducting polymer nanocavities. *Adv. Mater.* **33**, 2105004 (2021).

28. Xiong, K. et al. Video-rate switching of high-reflectivity hybrid cavities spanning all primary colors. *Adv. Mater.* **35**, 2302028 (2023)
29. Yang, L. et al. Rechargeable metasurfaces for dynamic color display based on a compositional and mechanical dual-altered mechanism. *Research* **2022**, 9870321 (2022).
30. Wang, G. et al. Mechanical chameleon through dynamic real-time plasmonic tuning. *ACS Nano* **10**, 1788–1794 (2016).
31. Ranjbar, S. et al. Smart chip for visual detection of bacteria using the electrochromic properties of polyaniline. *Anal. Chem.* **91**, 14960–14966 (2019).
32. Zhou, K. et al. Polyaniline films with modified nanostructure for bifunctional flexible multicolor electrochromic and supercapacitor applications. *Chem. Eng. J.* **345**, 290–299 (2018).
33. Zhang, S. et al. Solution-processable multicolor TiO_2/polyaniline nanocomposite for integrated bifunctional electrochromic energy storage device. *Appl. Surf. Sci.* **607**, 155015 (2023).
34. Franklin, D. et al. Actively addressed single pixel full-colour plasmonic display. *Nat. Commun.* **8**, 15209 (2017).
35. Ersman, P. A., Kawahara, J. & Berggren, M. Printed passive matrix addressed electrochromic displays. *Org. Electron.* **14**, 3371–3378 (2013).
36. Gugole, M. et al. Electrochromic inorganic nanostructures with high chromaticity and superior brightness. *Nano Lett.* **21**, 4343–4350 (2021).
37. Wang, Y. et al. Electrical tuning of phase-change antennas and metasurfaces. *Nat. Nanotechnol.* **16**, 667–672 (2021).